Materials Chemistry and Physics 305 (2023) 127856

Contents lists available at ScienceDirect

Materials Chemistry and Physics

journal homepage: www.elsevier.com/locate/matchemphys

Efficient antibacterial activity of ternary nanocomposites containing hydroxyapatite, Co_3O_4, and cerium oxide

Mohamed Ahmed [a,*], M. Afifi [a], Sherif Ashraf [b], Sahar A. Abdelbadie [c], Jonas Baltrusaitis [d]

[a] Faculty of Nanotechnology for Postgraduate Studies, Cairo University, El-Sheikh Zayed, 12588, Egypt
[b] Department of Physics, Faculty of Science, Suez University, Suez, 43518, Egypt
[c] Dar El-Salam Cancer Center, Ministry of Health, Cairo, Egypt
[d] Department of Chemical and Biomolecular Engineering, Lehigh University, 111 Research Drive, Bethlehem, PA, 18015, USA

HIGHLIGHTS

- TEM demonstrates HAP, and Co_3O_4 within GO with particle size of 8 nm for HAP.
- HAP/Co_3O_4/GO shows cell viability value of 97.9 ± 2.4%.
- The hardness value of HAP/Co_3O_4/GO composition is 4.1 ± 0.2 GPa.
- The antibacterial of HA/Ce_2O_3/GO are 15.9 ± 0.3, 16.4 ± 0.2 mm for *E. coli*, *S. aureus*.

ARTICLE INFO

Keywords:
Hydroxyapatite
Co_3O_4
Graphene oxide
Antibacterial
Hardness
Cerium oxide

ABSTRACT

Metal oxide nanoparticles are routinely utilized in the biomedical field due to their diverse functionality. In particular, hybrid nanocomposites containing metal oxides possess a significant tunability of their chemical properties, as well as modifiable grain size and morphology. Hydroxyapatite (HA) and graphene oxide (GO) are already widely used in bone tissue engineering. We hypothesized that the addition of cobalt oxide or cerium oxide to form a hybrid nanocomposite with HA and GO can further enhance their properties toward cell viability and biodegradability. In this work, cobalt oxide/cerium oxide were individually combined with HA and GO to fabricate a ternary nanocomposite - HA/Co_3O_4/GO and HA/CeO_2/GO for its potential use as a bone replacement hybrid material. The crystal structure of the resulting HA/Co_3O_4/GO composite was elucidated with XRD. The surface composition of the composite was analyzed using X-ray Photoelectron Spectroscopy and complex surface speciation was observed and assigned to $Co(OH)_2$ and Co_3O_4. The particle length of HA in the composite was 35.5 ± 7.0 nm while the particle size of the cubic Co_3O_4 was 49.3 ± 10.8 nm, as revealed in TEM images. The antibacterial properties of HA/CeO_2/GO were measured with the resulting inhibition area for *E. coli* and *S. aureus* of 15.9 ± 0.3 mm and 16.4 ± 0.2 mm, respectively. The ternary composite of HA/CeO_2/GO and HA/Co_3O_4/GO showed an improvement in hardness of 4.1 ± 0.2 GPa and 3.2 ± 0.2. Summarily, HA/Co_3O_4/GO exhibited improved porosity, cell viability, and biodegradability compared with pristine HA. Overall, HA/Co_3O_4/GO nanocomposite possessed a porous structure and showed excellent antibacterial properties as well as controlled biodegradability and can be proposed as an improved bone-implant biomaterial.

1. Introduction

Nanotechnology is widely utilized in a plethora of clinical applications owing to its ability to yield controlled grain size, macrostructure, chemical composition and topology of the resulting nano-bio materials [1]. Globally, bone defects affect the human quality of life, especially in the geriatric age group [2]. Intrinsically, human bodies contain bioceramic materials, in addition to numerous metals [3]. Most biomaterials that are used in bone engineering applications consist of metals or metal oxides as well as calcium phosphate – hydroxyapatite (HA) [3]. This combination is used to combine the high mechanical strength of metal oxides and the similarity of hydroxyapatite to the bone

* Corresponding author.
E-mail address: m.khalaf@sci.suezuni.edu.eg (M. Ahmed).

https://doi.org/10.1016/j.matchemphys.2023.127856
Received 28 August 2022; Received in revised form 22 April 2023; Accepted 30 April 2023
Available online 1 May 2023
0254-0584/

apatite resulting in composites of better biocompatibility, biodegradability and other integral properties that suit bone applications [4]. Finally, graphene oxide (GO) sheets are also combined with biomaterials and used in hard tissue engineering [5].

HA is a ceramic material that possesses a high propensity for hybridization with other materials, especially when formulated as nanoparticles, due to its physical and chemical properties, especially the ability to be substituted by various ions [6]. Biomaterials containing HA showed remarkable biocompatibility properties due to their structural resemblance to the natural apatite [7]. Adding metal ions, such as cobalt, to HA yields a hard-tissue implant with the solidity advantage, in addition to its stability in the biological fluids [8]. It was previously shown that adding HA to graphene oxide sheets improved mechanical strength and altered the surface roughness of the resulting biomaterial leading to a more biocompatible composite. Moreover, Y. Zeng et al. studied the mechanical parameters and biocompatibility of the HA/GO composite [9]. They revealed that composite structure was strengthened upon incorporating HA into GO sheets and its biocompatibility remarkably improved.

Graphene oxide (GO) is a single layer of sp^2 carbons bonded in a form of a honeycomb structure [10]. GO is characterized as a safe, inexpensive and biocompatible biomaterial [11]. It showed interesting properties in biomedical application studies due to its surface oxygenated functional groups and its aromatic nature that enhanced biocompatibility and biodegradability [12]. Combining GO and HA for biomedical applications was studied by Yao et al. [13]. They showed that adding HA to GO resulted in a bioactive and biocompatible composite due to the alteration of its surface roughness that occurred after HA addition. Further, Shin et al. studied the application of HA/GO composite in bone engineering and illustrated that the osteogenesis process was remarkably enhanced when combining GO and HA [14].

The highly oxygenated metal oxide is able to release reactive oxygen species (ROS) which may clarify the advances in the antibacterial capability. ROS includes superoxide radicals such as (O^{-2}), (OH^-) and active hydrogen peroxide H_2O_2 [15]. Undeniably, metals oxides discharge oxonium ions (H_3O^+), which directly interrupted antimicrobial resistance owing to causing change in cellular pH [16]. Thus, cerium oxide (CeO_2) reversible redox reaction of the Ce^{4+}/Ce^{3+} couple regulates the antioxidant behavior of cerium oxide with potential uses in medicine, acting a vital role as a cell shield against oxidative stress, besides its usage as a sensitizer in cancer radiotherapy/antibacterial claims [17]. The performance of cerium oxide depends on its ability to coordinate oxygen species, but also the redox exchanging process $Ce^{4+} \leftrightarrow Ce^{3+}$. Nevertheless, these introduced characteristics are in close connection with lattice defects, such as oxygen vacancies, leading to unusual coordination. All these features cause a higher reactivity. Consequently, defect engineering has been concerned with manipulating the surface chemistry of cerium oxide. In addition, oxygen vacancies act a crucial role as antioxidant activity [17].

On the other hand, cobalt oxide is an abundant and inexpensive transition metal oxide [18]. Cobalt has various oxidation states and possesses specific physical and chemical properties to be utilized in many biomedical applications [19]. Many studies demonstrated the success of implanting orthopedic biomaterials containing cobalt due to the stimulation of the angiogenesis process and the enhancement of the oxygen supply [20]. The objective of the present study is to formulate a ternary nanocomposite consisting of HA, Co_3O_4 and GO nanosheets, as each component was already used separately and in binary mixtures in previous studies related to bone-implant applications and the results revealed their ability to improve bone repair. The resulting composite was characterized using different analytical methods to confirm the presence of the constituent crystalline phases of HA/Co_3O_4/GO in the composite. Experiments to demonstrate the relevance of the resulting composite for biomedical applications, e.g. evaluation of cell viability, antimicrobial activity, and corrosion stability, were also conducted.

2. Experimental and methods

2.1. Materials

Calcium chloride, diammonium phosphate, cobalt oxide, cerium oxide, potassium permanganate, graphite, and hydrochloric acid were obtained from LOBA, India, and were used as received.

2.2. Synthesis procedure

The synthesis of HA and GO was performed separately. Firstly, HA was synthesized by mixing 100 ml of deionized water (DIW), 0.5 M of $CaCl_2{\cdot}2H_2O$ and 0.3 M of $(NH_4)_2HPO_4$ with diluted ammonia used to maintain the solution pH at 11 ± 0.1. The mixture was stirred for 2 h using a magnetic stirrer at 1200 rpm. Afterward, the solution was aged for 24 h, and the precipitated gel was filtered and washed with DIW. Finally, the filtered gel was dried in the drier furnace at 50–60 °C.

Secondly, GO was synthesized using the modified Hummers' method. 5 g of graphite was added to 120 ml of H_2SO_4 and mixed vigorously for 30 min. Afterward, 12 g of $KMnO_4$ was added to the graphite vessel and stirred for 2 h followed by 300 ml of DIW with a rate of 10 ml/h to avoid a temperature rise. The mixture was cooled, then 10 ml of H_2O_2 was added dropwise. The resulting solution was stirred vigorously for 30 min. The mixture was filtered and disperse several times in 500 ml of HCl (20 wt %) solution using an ultrasonic probe for 15 min, then the filtrate was dried at 50–60 °C in a drying furnace.

Thirdly, the following six nanocomposites were prepared. Namely, nanocomposites containing parent materials, binary mixtures and ternary mixture were prepared as follows: pure Co_3O_4, pure CeO_2, HA: Co_3O_4=(1:1), HA: CeO_2=(1:1), HA: Co_3O_4:GO=(1:1:0.05), HA: CeO_2: GO =(1:1:0.05),. Weighed materials were added to 50 ml of DIW sonicated for 15 min in the probe sonicator to evenly disperse the solution, then centrifuged at 6000 rpm for 10 min to collect the resulting powder sample composite materials. Lastly, the samples were dried for several hours at 50–60 °C. The overall synthesis procedure is summarized in Fig. 1.

2.3. XRD analysis

The Pertpro, USA diffractometer equipped with Cu $k_{\alpha 1}$ radiation (λ = 1.5404 Å) operating at 45 kV and 40 mA was used to record X-ray diffraction (XRD) patterns.

2.4. FTIR measurements

The Fourier transformed infrared (FT-IR) spectra were acquired using PerkinElmer 2000 spectrometer in the 4000–400 cm^{-1} range using transmittance mode. The powdered samples were mixed with KBr for dilution.

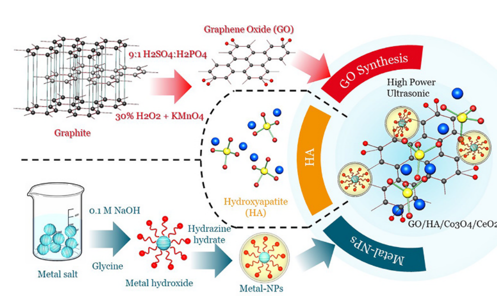

Fig. 1. Schematic diagram showing the synthesis procedure of the HAP/Co_3O_4/GO nanocomposite.

2.5. X-ray Photoelectron Spectroscopy (XPS) measurements

XPS was performed using K-ALPHA instrument (Themo Fisher Scientific, USA) utilizing monochromatic X-ray Al Kα radiation in the range of 10–1350 eV, spot size 400 μm operating at pressure 10^{-9} mbar with full spectrum pass energy of 200 eV and that of high resolution spectrum of 50 eV. CasaXPS 2.3.23PR1.0 was used for data processing [21]. All spectra were calibrated to C1s peak at 285.0 eV. Quantification was performed using Scofield relative sensitivity factors and assuming constant instrument transmission [22].

2.6. Field emission scanning electron microscopy (FESEM)

The reported surface morphology and roughness were obtained using a ZEISS) scanning electron microscope. Moreover, Energy dispersive X-ray (EDX) was performed using the same SEM instrument.

2.7. In vitro cell viability tests

The human osteoblast cell line was used to evaluate the cell viability after culturing in Dulbecco's modified Eagle's medium (DMEM, Gibco) at 37 °C and in the presence of 5% CO_2. A serialized 96 well plate containing 5 mg of each sample was prepared by maintaining the cell density of about 5×10^3 cells/cm^2. Thereafter, the medium was removed after incubation for 3 days and (3-(4,5-dimethylthiazol-2-yl)-2,5-diphenyltetrazolium bromide) (MTT) was added. MTT acts to interact with the cells to differentiate between the living and the deals ones. Therefore, it was added to each well and the optical analyzer was used to detect cell viability. The statistical analysis was performed using Medcalc software version 15.0 (Mariakerke). The continuous variables were represented using a mean standard deviation (SD).

2.8. Antibacterial activity

The antibacterial activity of the different samples was evaluated using the diffusion desk technique. The test was done using two bacteria (*Staphylococcus aureus* = *S. aureus*), and (*Escherichia coli* = *E. coli*), which were purchased from American Type Culture Collection (ATCC) Number 29213, and ATCC number 25922, respectively. The powdered sample's initial concentration was about 20 mg/ml. The samples were exposed to the two pathogens for 24 h then the obtained inhibition zone was measured in mm. To calculate standard deviation values, the experiment was repeated three times.

2.9. Hardness

TTS UNLIMITED INC. model: HWDM-7/Japan was used to evaluate the hardness with *in situ* imaging mode.

2.10. Ionic release

The concentration of released ions was measured by immersing the sample in 100 ml of simulated body fluid (SBF). Inductively coupled plasma (ICP) spectroscopy (720 ICP-OES, Agilent Technologies, USA) was used for the elemental analysis of the resulting SBF. The experiments were repeated three times.

3. Results and discussion

3.1. Crystalline phase identification

XRD patterns of parent HA, Co_3O_4 and the resulting binary and ternary nanocomposites with GO are shown in Fig. 2. In particular, XRD shows the change in the structural arrangement of parent material in the different formulation composites [23]. The diffraction patterns showed sharp peaks for the cubic crystalline structure of Co_3O_4 [24]. All XRD

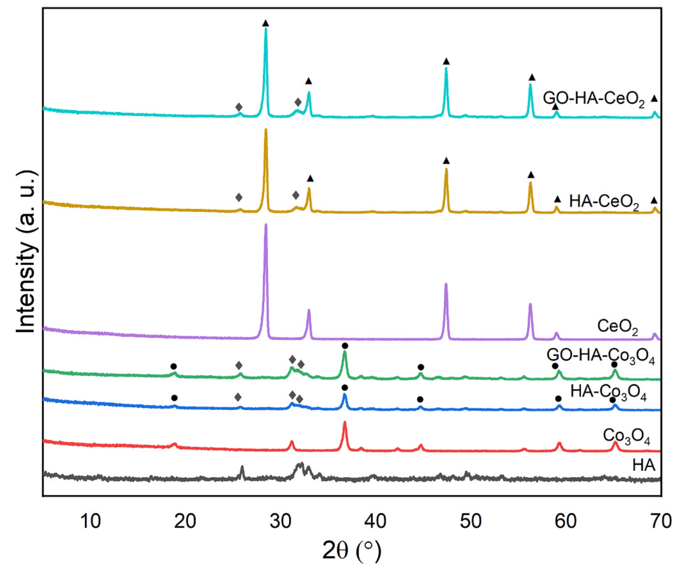

Fig. 2. XRD pattern of different nanocomposites: Co_3O_4, HA-Co_3O_4, GO-HA-Co_3O_4, CeO_2, HA- CeO_2 and GO-HA- CeO_2 in which (◆) HAP, (•) Co_3O_4 and (▲) CeO_2.

peaks of Co_3O_4 were sharp and maintained their sharpness upon the addition of GO and HA suggesting a highly crystalline structure of Co_3O_4 [25]. The sharp peak of (311) plane of Co_3O_4 that appeared in the Co_3O_4, HA/Co_3O_4 and HA/Co_3O_4/GO pattern represent the preference of Co_3O_4 crystal growth in this plane [26]. The specific hexagonal crystal structure of HA was exhibited with the peaks at 25°, 31.5°, 33.2°, 46.7°, 49.9°, and 53.1° attributed to (002), (211), (300), (222), (213), and (004) planes [27]. The significant peak of GO seems to be lowered in the patterns of composite materials. The CeO_2 is confirmed with the diffraction peaks at 29°, 32°, 46°, 55°, 60° [28]. It can be noticed that GO peaks are not separated with respect to the other components, which might be attributed to its poor crystallinity in addition to the low quantity of GO in the nanocomposites. The HA/CeO_2/GO displays noisy/wide peaks that refer to crystallinity disturbance upon its formation [29]. Therefore, these crystalline defects play a significant role as active sites in composite applicability.

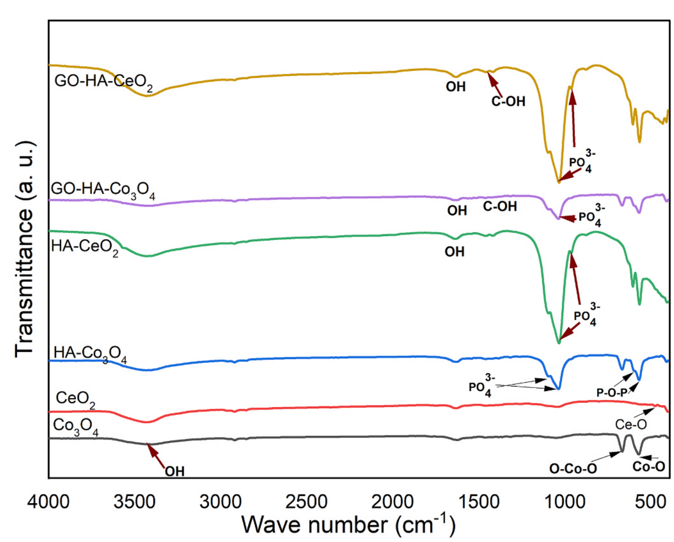

Fig. 3. FTIR spectrum of Co_3O_4, HA-Co_3O_4, GO-HA-Co_3O_4, CeO_2, HA- CeO_2 and GO-HA- CeO_2.

3.2. FTIR spectra

FTIR of the nanocomposites are demonstrated in Fig. 3, whilst the bands are found in Table 1. The band of 474 cm^{-1} is attributed the existence of Ce–O vibrational bond [30]. Moreover, the sharp bands at 1033-1037 cm^{-1} are attributed to the (ν_3) stretching mode of PO_4^{3-} group [31,32], while the bands of 565–606 cm^{-1} are accompanied to the bending mode of vibrational PO_4^{3-} group belong to HA structure [31,32]. Moreover, the peak that appeared at 665 cm^{-1} was associated with O–Co–O [33,34]. The bands of 1408 and 1405 cm^{-1} refer to the C–OH stretching mode which might belong to the GO structure [35]. Furthermore, the bands of 1642 cm^{-1} and 3420 cm^{-1} are assigned to the O–H vibrational mode. Thus, the most constituents that have been involved in the composites were detected through the FTIR vibrational modes.

3.3. XPS spectra

Fig. 4 shows the survey and high-resolution XPS scans for HA/Co_3O_4/GO nanocomposite. XPS is commonly used for analyzing composite materials and identifying their valence; it also is used to suggest an even distribution of each nanoparticle within the composite [39]. The presence of Ca, O, P, Co, and C are demonstrated by the survey scan in Fig. 4. In particular, a doublet with the main Co2$p_{3/2}$ peak located at 780.5 eV structure represents a mixture of Co_3O_4 with an overlayer of Co$(OH)_2$ formed under a moist environment [40]. This is supported by the O1s peak at 532.0 eV C1s spectrum exhibited the main peak at 285.0 eV with some oxidized carbon groups at 289.2 eV attributable to a complex surface layer partially comprised of calcium carbonate [41]. The surface of the HA/Co_3O_4/GO nanocomposite also contained considerable amounts of calcium and phosphorus. In particular, the resulting XPS elemental quantification performed resulted in 12% carbon, 12% calcium, 8% cobalt, 56% oxygen and 10% phosphorus.

3.4. Morphological features

TEM micrographs of all binary and ternary nanocomposite materials are in Fig. 5a-d. Fig. 5a displays the crystalline cubes of Co_3O_4 where the dark cubes of Co_3O_4 are in contact with the HA rods. This morphology elucidation is related to the difference in mass and electron density between Co_3O_4 and HA [42] The average size of 49.3 ± 10.8 nm for Co_3O_4, while 12.2 ± 4.3 nm size and 35.5 ± 7.0 nm length for HA. Fig. 5b shows the morphological pattern of HA/Co_3O_4/GO that reveals the embedding of Co_3O_4 particles and HA within GO sheets. This even scattering of HA, and Co_3O_4 within GO yields an integrated nanocomposite and strengthens its structure [43]. The HA/CeO_2 binary nanocomposite demonstrates HA grains with higher average length (110 nm) in comparison with CeO_2 grains (33 nm), however, it takes the same displayed shape as shown in Fig. 5c. Finally, the combination of the triple compositions in one composite shows a great improvement in raising surface area due to the significant decline in aggregation tendency as it is illustrated in Fig. 5d.

SEM micrographs for all composites are shown in Fig. 6a-f. Fig. 6a demonstrates a cotton-like shape of HA/Co_3O_4 composite showing distinct incisions associated with the additional Co_3O_4 to HA in which HA diameter reduced to 8–14 nm and length is 35–40 nm while Co_3O_4 shows a particle size of 3–11 nm. Moreover, Fig. 6b–c represents the triple nanocomposite topological changes, showing even incorporation of HA and Co_3O_4 on top of the GO surface. In addition, the reduced grain size is explained by SEM which agrees with TEM graphs. Fig. 6d exhibits the homogeneous distribution of HA grains upon CeO_2. The HA/CeO_2 grains have appeared in a smaller size that offers a higher surface area. Moreover, the ternary composite is shown in Fig. 6f with clear GO folds and noticed decreasing in HA and CeO_2 grains aggregates.

SEM analysis also can provide information about the surface roughness in a qualitative insight. The surface roughness of the nanocomposites is discussed to assess their appropriateness in biomedical applications. The roughness increased in the ternary nanocomposites due to various factors such as reduction in size or inhomogeneous distribution which creates valley depth and heights. Additionally, the porous nature of the ternary nanocomposites may enable the movement of nutrients and oxygen to enhance osteoblast growth. According to these results, the ternary nanocomposites have improved porosity structure and integrated rough surfaces making them suitable for bone implant applications.

Table 1
FTIR bands for all samples upon their bands' assignments.

Co_3O_4	CeO_2	HA/Co_3O_4	HA/CeO_2	HA/Co_3O_4/GO	HA/CeO_2/GO	Assignment	Ref.
–	474	–	–	–	–	Ce–O vibration	[30]
570	–	–	–	574	–	Co–O	[36]
–	–	568	566	568	565	PO_4^{3-} bending (ν_4)	[31, 32]
–	–	602	606	602	602	PO_4^{3-} bending (ν_4)	[31, 32]
665	–	666	–	666	–	O–Co–O (vibrations at a tetrahedral site)	[33, 34]
–	–	969	962	–	962	PO_4^{3-} stretching (ν_1)	[31, 37, 38]
–	–	1037	1034	1032	1033	PO_4^{3-} stretching (ν_3)	[31, 32]
–	–	–	–	1405	1408	C–OH stretching	[35]
1624	1631	1629	1637	1628	1631	Water absorbed	[31]
3420	3432	3434	3434	3433	3434	O–H stretching	[25]

3.5. EDX analysis

EDX scan was done to confirm the bulk elemental composites of HA/Co_3O_4/GO and HA/CeO_2/GO nanocomposites. Fig. 7a-b demonstrates the EDX spectrum that reveals peaks that confirmed the presence of elemental components. Table 2 shows the elemental composite. In agreement with XRD and FTIR results, EDX suggests the presence of the three components, HA, Co_3O_4, CeO_2, and GO, in the composite material.

EDX is routinely used to investigate the spatially-resolved elemental composition. The atomic ratio in EDX denotes the ratio of the bulk chemical composition. On the other hand, the atomic ratio in XPS for each element and its fragments are assigned to their surface concentration. The difference between EDX and XPS can thus be assigned to the compositional differences between the bulk and the surface. These, in turn, can be affected by the homogeneity of the composite material component distribution, as well as the spatial resolution of the instrument (EDX usually can analyze the composition from a small electron beam scanned area whereas XPS analyses much larger, averaged, area of the sample surface. Using this perspective, the results shown in Table 2 can be compared with those described in XPS analysis section 3.3 for atomic compositions. It can be seen that the surface of the composite material is enriched in HA and cobalt components showing Co_3O_4 with HA binding to the surface of GO and partially covering it.

3.6. Cell viability

The samples' cell viability was assessed using in vitro cell lines. The

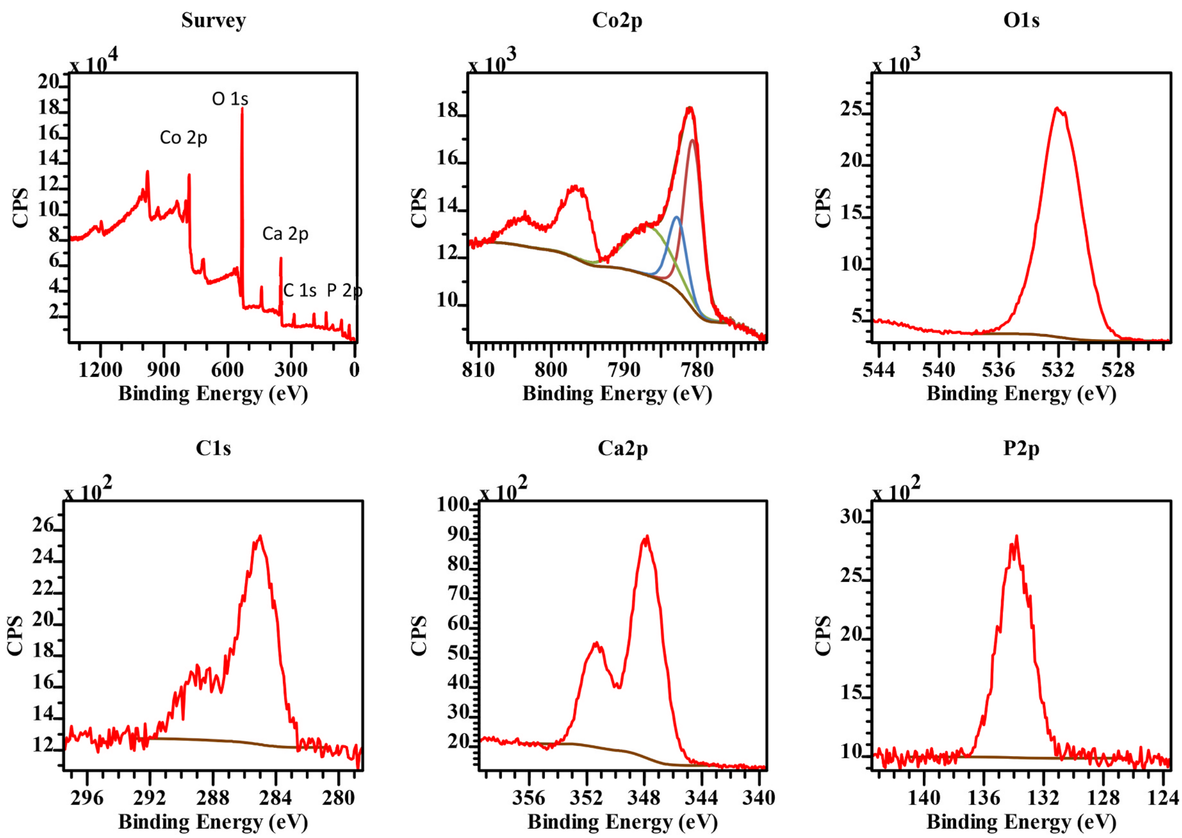

Fig. 4. XPS spectra of the nanocomposite HAP/Co_3O_4/GO including survey, Co2p, O1s, C1s, Ca2p and P2p high resolution spectra.

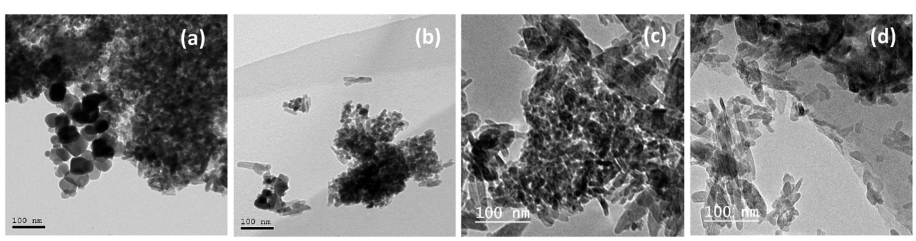

Fig. 5. TEM micrographs of nanocomposites; (a) HA-Co_3O_4, (b) GO-HA-Co_3O_4, (c) HA- CeO_2, and (d) GO-HA- CeO_2.

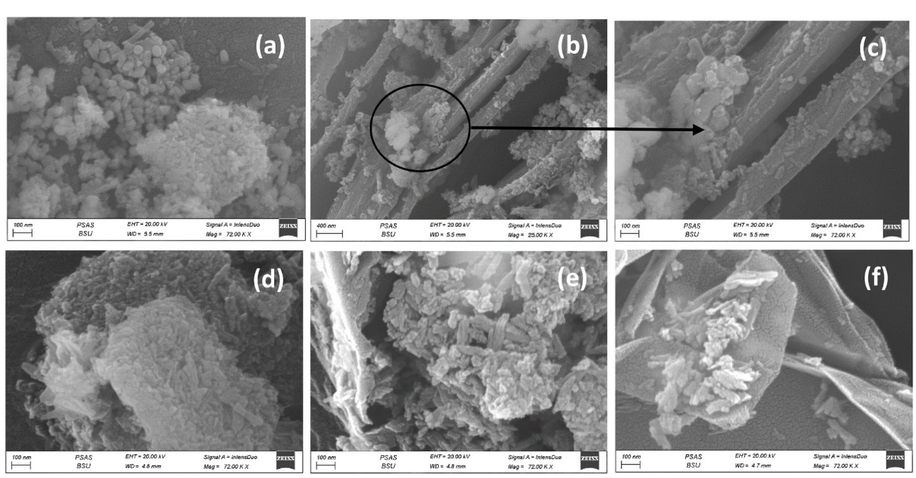

Fig. 6. SEM micrographs: (a) HA- Co_3O_4, (b, c) GO-HA-Co_3O_4, and (d) HA-CeO_2, (e) GO-HA, (f) GO-HA- CeO_2.

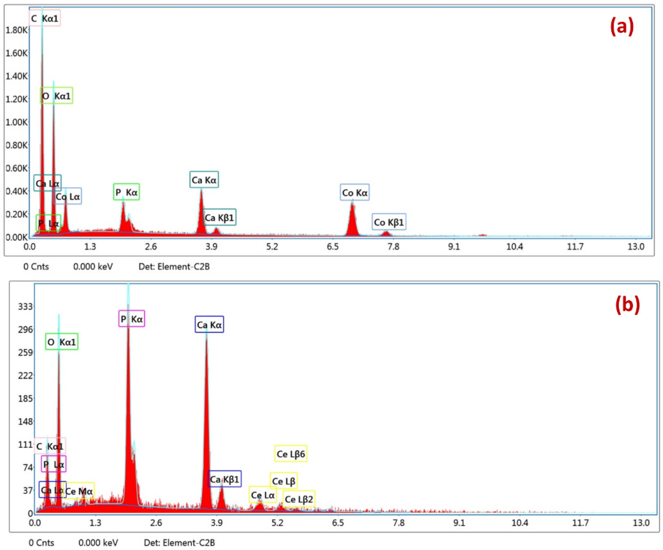

Fig. 7. EDX spectrum of (a) GO-HA-Co_3O_4 and (b) GO-HA-CeO_2 nanocomposite.

Table 2
Elemental composite of HA/Co_3O_4/GO and HA/CeO_2/GO composites.

Element	Weight %		Atomic %	
	HA/Co_3O_4/GO	HA/CeO_2/GO	HA/Co_3O_4/GO	HA/CeO_2/GO
C	39.5	12.12	55.6	21.65
O	32.7	38.91	34.6	52.17
P	3.2	16.71	1.8	11.58
Ca	7.6	25.3	3.2	13.54
Co	17.0	0.0	4.9	0.0
CeL	0.0	6.96	0.0	1.07

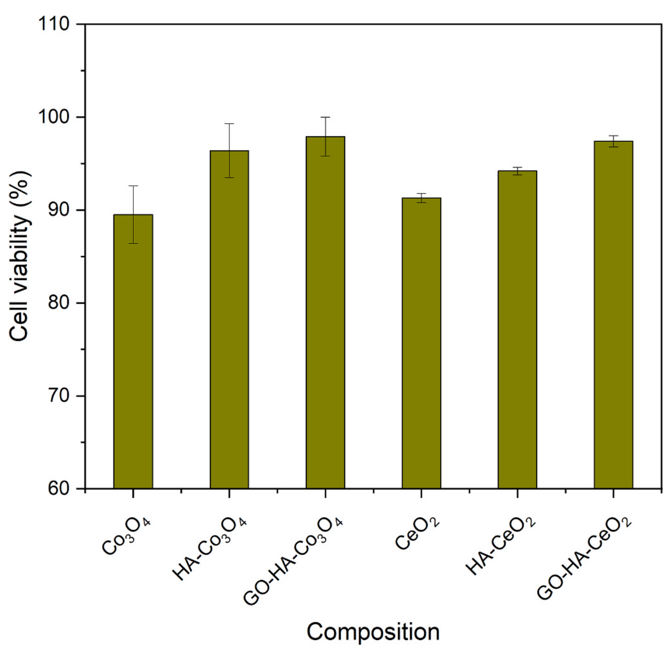

Fig. 8. Cell viability of human osteoblasts cell lines of Co_3O_4, HA-Co_3O_4, GO-HA-Co_3O_4, CeO_2, HA- CeO_2 and GO-HA- CeO_2.

cell viability data for each nanocomposite are shown in Fig. 8. Because of its closeness to genuine bone apatite, HA has a high cell survival of 95.7 ± 2.5%. However, Co_3O_4 has a lower survivability value of 89.53% compared to HA. Furthermore, combining Co_3O_4 with HA resulted in a 96.4 ± 2.8% increase in cell survival. Adding Co_3O_4 and HA to GO sheets increased the biocompatibility of this composite material, according to the improved viability values. HA into GO nanosheets improved cell viability, according to J. Jyoti et al. [44]. They reported that HA/GO composites had a high survivability value of about 95%, with improved bioactivity and osteoinductivity owing to the altered porosity of the structure. The high biocompatibility of these phases, as seen by the low change in viability between them, is a critical feature for their use in medical applications. As a result, combining HA and Co_3O_4 with GO to make HA/Co_3O_4/GO a viable option for bone replacement research. However, the cell viability of cerium trioxide compound (CeO_2) occupied the value of 91.3 ± 0.5%. The binary NC of HA/CeO_2 persuades mineral trioxide viability percentage, reaching 94.2 ± 0.4%. In addition, The disadvantage of nano-material usage in biological applications is hydrophilicity and introducing significant stability in dispersion [45]. Correspondingly, GO nanosheets introduce an electronegative surface, causing electrostatic repulsion, hence a stable aqueous suspension might be obtained [45]. As a result, combining the three ingredients hits the peak cell viability % at 97.4 ± 0.6%.

3.7. Ionic release

The assessment of ion release was done by immersing HA/Co_3O_4/GO composite in (SBF) simulated body fluids at 37 °C for 24 h. Fig. 9 demonstrates the release of cobalt and calcium ions from HA/Co_3O_4/GO over 24 h. The release of Ca and Co ions within the first 4 h was relatively high due to the dispersion of ions from the nanocomposite surface via the diffusion method. After that, the ions diffused over the time from nanocomposite core. Hence, this step depends not only on diffusion but also on dissolution and controlled biodegradability rate of HA/Co_3O_4/GO which consequently shows the reasonable continuous release of ions over hours as shown in the plot. The presence of Co^{2+} ions with a high concentration in biological fluids cause toxicity, consequently, the proper degradability of biomaterials containing Co ions should be taken into consideration [46]. The combination of cobalt and hydroxyapatite shows a controlled release of Co^{2+} ions, owing to the decreased ability of HA to substitute Co^{2+} ions which creates a suitable interaction between Co_3O_4 and HA in addition to the managed ion release [47]. The ion burst release phenomenon can disrupt the efficiency of the biomaterial and cause toxicity, hence, a hybrid composite with a porous integrated structure shows a controlled release of ions lowering the risk of showing

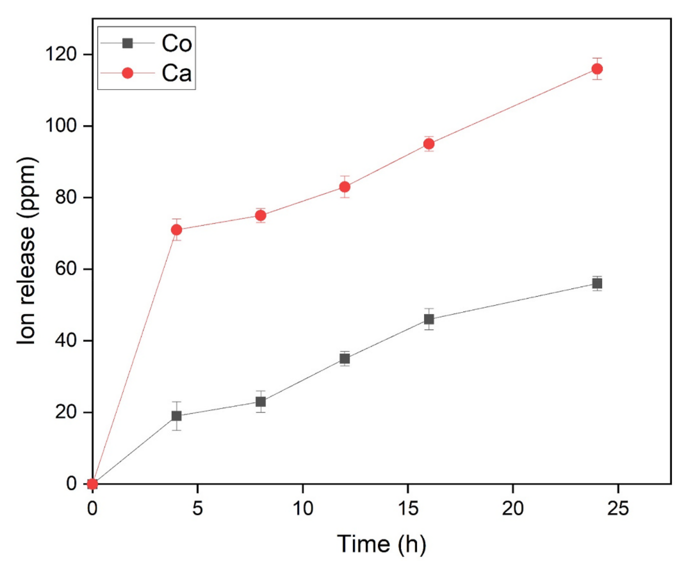

Fig. 9. Elemental concentrations in simulated body fluid (SBF) over time for nanocomposite HAP/Co_3O_4/GO.

this phenomenon [48]. Therefore, HA/Co_3O_4/GO nanocomposite has a controlled biodegradability which is confirmed with ionic release analysis.

The releasing of ions from nanocomposites is critical in biomedical applications since excessive ion release can induce cytotoxicity and damage to the biomaterial's efficiency. The chemical degradation of the material is directly related to the ionic release measurement. Moreover, the ion concentration discharged may have an effect on the surrounding biological environment causing cellular toxicity or inflammation. As a result, the ability to control and manage the released ion is critical for the development of safe and efficient biomaterial.

3.8. Antibacterial properties

The bacterial toxicity was evaluated against two pathogens, e.g. *E. coli* and *S. aureus*. Fig. 10 demonstrates the toxicity exerted against these two bacteria in the form of an inhibition zone measured in mm. Notably, HA shows almost no toxic effect, whereas Co_3O_4 shows toxicity of 11.2 ± 0.8 and 11.6 ± 0.7 mm against *E. coli* and *S. aureus*. Adding HA to Co_3O_4 shows a significant improvement in bacterial toxicity of 12.3 ± 0.6 and 12.6 ± 08 mm. The cerium oxide CeO_2 compound shows accepted antibacterial performance against both E.coli with inhibition zone 8.4 ± 0.3 mm, and *S. aureus* zone 8.5 ± 0.1 mm. The maximum exerted toxicity is obtained by HA/Co_3O_4/GO composite of 13.1 ± 0.9 mm and 14.1 ± 0.9 mm. This demonstrates the synergistic antibacterial activity of HA/Co_3O_4/GO which agrees with literature reports. In particular, Mazinani et al. studied the antimicrobial effect of GO [49]. They revealed that the bacterial toxicity of GO was exhibited via the formation of reactive oxygen species (ROS). Oxygenated functional groups of GO interact with the cell membranes of bacteria and damage the membrane resulting in cell death. The antibacterial activity of bone-implant biomaterials aids in speeding up the bone-repair process by avoiding infections that would otherwise slow its healing down [50]. Further, the mineral oxide's antibacterial actions are tightly bonded to the released oxonium ions (H_3O^+) which act a vital role in interrupting the living cells' pH, as well as bacterial reproduction, and hence inhibit drug-resistant phenomenon [16]. Consequently, the binary nano-composite HA/CeO_2 breaks bacterial spread and reproduction in a wider zone of 11.3 ± 0.4 mm in case of *E. coli*, while it is 11.9 ± 0.2 mm in the case of *S. aureus*. Krishnamoorthy et al., 2014 elucidated the GO mechanism against bacterial growth via ROS and trapping of pathogenic species within the graphene oxide wafers [45]. Inclusion of the three ingredients in a single TNC hits the peak antibacterial values with 15.9 ± 0.3 mm for E.coli and 16.4 ± 0.2 mm for *S. aureus*. Further, reactive species praise such nano-compositions for drug delivery applicability [51].

Antibacterial activity is a crucial property for nanocomposites intended for implant applications because the bacterial infection is a significant concern in implant surgery. Bacterial colonization of the implant surface can lead to implant failure, prolonged hospitalization, and even life-threatening conditions. Therefore, developing implant materials with inherent antibacterial properties is essential to prevent bacterial colonization and ensure the long-term success of the implant [52,53]. Nanocomposites with antibacterial properties can inhibit bacterial growth, adhesion, and colonization, providing a protective barrier against infection. Moreover, the use of nanocomposites with antibacterial properties can reduce the dependence on antibiotics, which can lead to antibiotic resistance.

3.9. Hardness

The strength of the samples is evaluated by a hardness study. Fig. 11 shows the hardness plot. Hardness evaluation is important in most bone tissue applications [54]. For pure CeO_2, the microhardness is 2.4 ± 0.2 GPa, while for Co_3O_4 without any modifications is around 2.1 ± 0.3 GPa. The combination of HA with CeO_2 and Co_3O_4 in binary nanocomposites showed enhancement in the values reached 2.7 ± 0.2 and 2.6 ± 0.3 GPa respectively. Further, the TNC HA/CeO_2/GO occupied the uppermost micro-hardness in the group of CeO_2 with 3.2 ± 0.2 GPa. Moreover, HA/Co_3O_4/GO composite obtains the maximum hardness value of 4.1 ± 0.2 GPa. This high hardness value of HA/Co_3O_4/GO indicates that Co_3O_4 and GO reinforced the HA structure resulting in the improvement of structural strength. The even distribution and the proper interaction between Co_3O_4, GO, and HA results in an integrated structure that can be suggested as a bone implant [55]. Observably, the resultant data confirms the reinforcement effect of GO ingredients that boosts interfacial bonding between the formed composites' raw constituents [56]. The bone implant's mechanical properties are significant

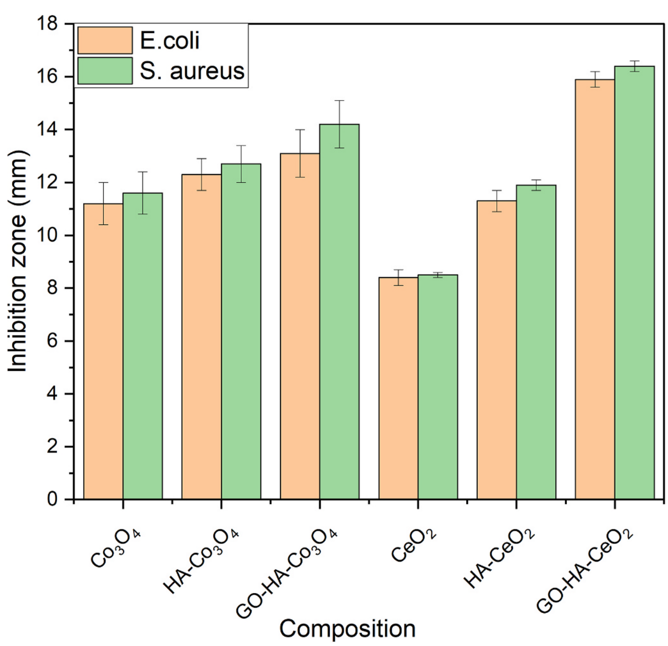

Fig. 10. Antibacterial activity against *E. coli* and *S. aureus* of Co_3O_4, HA-Co_3O_4, GO-HA-Co_3O_4, CeO_2, HA- CeO_2 and GO-HA- CeO_2.

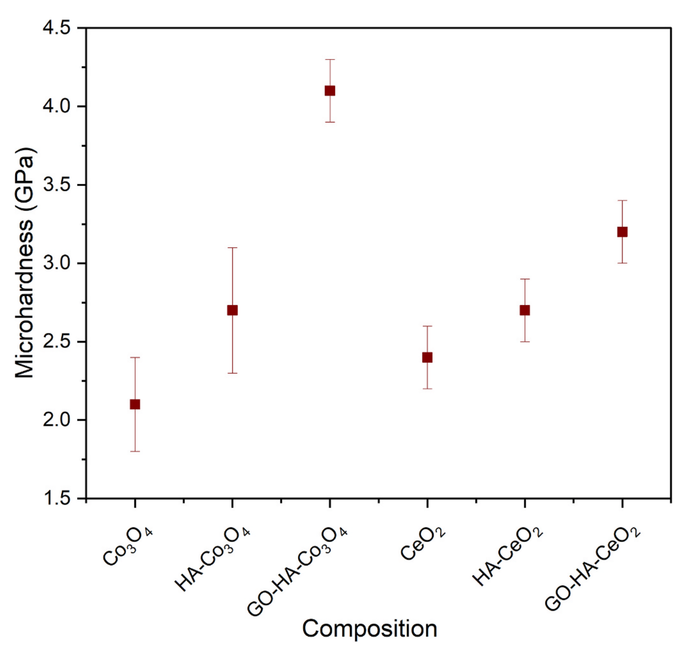

Fig. 11. Hardness graph for different nanocomposites: Co_3O_4, HA-Co_3O_4, GO-HA-Co_3O_4, CeO_2, HA- CeO_2 and GO-HA- CeO_2.

for its effectiveness, especially over a long period. The potential implant material should tolerate mechanical loads and body stresses without breaking or deforming like the natural bone. As a result, bone implant design should sustain appropriate mechanical behavior for higher integration with the host tissue.

4. Conclusions

Different nanocomposites including HA/Co_3O_4, HA/Co_3O_4/GO, HA/CeO_2, and HA/CeO_2/GO were synthesized and analyzed. XRD revealed the crystalline alteration within the nanocomposite structure. The embedding of HA and Co_3O_4 or CeO_2 into GO was demonstrated using TEM micrographs showing an average grain size reached 8 nm and length of 20 nm for HA and 8 nm size for Co_3O_4. Moreover, HA/Co_3O_4/GO and HA/CeO_2/GO showed an improved cell viability value of 97.9 ± 2.4% and 97.4 ± 0.6% respectively. Furthermore, the antibacterial activity of HA/Co_3O_4/GO and HA/CeO_2/GO was evaluated against *E. coli* and *S. aureus*, with the activity of 13.1 ± 0.9 mm and 14.1 ± 0.9 mm for the cobalt-based nanocomposite and 15.9 ± 0.3 and 16.4 ± 0.2 mm for the cerium based one. The maximum hardness value was reached by two ternary nanocomposites with values of 4.1 ± 0.2 and 3.2 ± 0.2 GPa. Finally, the ternary nanocomposites are integrated and porous structures with excellent roughness and mechanical properties that showed improved cell viability, in addition to enhanced antibacterial activity. Since ternary nanocomposites exhibited better biocompatible and biodegradable properties than binary composites. Therefore, it can be suggested for future clinical examinations for more bone engineering studies.

CRediT authorship contribution statement

Mohamed Ahmed: Conceptualization, Writing – review & editing. **M. Afifi:** Methodology, Software, Writing - review & editing. **Sherif Ashraf:** Writing – original draft. **Sahar A. Abdelbadie:** Data curation, Formal analysis, Investigation. **Jonas Baltrusaitis:** Supervision, Project administration, Formal analysis, Methodology, Validation, Writing - review & editing.

Declaration of competing interest

The authors declare that they have no known competing financial interests or personal relationships that could have appeared to influence the work reported in this paper.

Data availability

Data will be made available on request.

Acknowledgments

This material is based upon work supported by the USA National Science Foundation under Grant No. CHE 1710120.

References

[1] M. Amiri, A. Akbari, M. Ahmadi, A. Pardakhti, M. Salavati-Niasari, Synthesis and in vitro evaluation of a novel magnetic drug delivery system; proecological method for the preparation of CoFe2O4 nanostructures, J. Mol. Liq. 249 (2018) 1151–1160.

[2] M. Alizadeh-Osgouei, Y. Li, C. Wen, A comprehensive review of biodegradable synthetic polymer-ceramic composites and their manufacture for biomedical applications, Bioact. Mater. 4 (2019) 22–36.

[3] A. Ressler, A. Zu_zi, I. Ivani_sevi, N. Kamboj, H. Ivankovi, Ionic substituted hydroxyapatite for bone regeneration applications: a review, Open Ceramics 6 (2021), 100122.

[4] N.K. Awad, S.L. Edwards, Y.S. Morsi, A review of TiO2 NTs on Ti metal: electrochemical synthesis, functionalization and potential use as bone implants, Mater. Sci. Eng. C Mater. Biol. Appl. 76 (2017) 1401–1412.

[5] Z. Fan, J. Wang, Z. Wang, H. Ran, Y. Li, L. Niu, et al., One-pot synthesis of graphene/hydroxyapatite nanorod composite for tissue engineering, Carbon 66 (2014) 407–416.

[6] Y. Zhang, Z. Li, W. Sun, C. Xia, A magnetically recyclable heterogeneous catalyst: cobalt nano-oxide supported on hydroxyapatite-encapsulated γ-Fe2O3 nanocrystallites for highly efficient olefin oxidation with H2O2, Catal. Commun. 10 (2008) 237–242.

[7] Z. Abdel-Hamid, M.M. Rashad, S.M. Mahmoud, A.T. Kandil, Electrochemical hydroxyapatite-cobalt ferrite nanocomposite coatings as well hyperthermia treatment of cancer, Mater. Sci. Eng. C Mater. Biol. Appl. 76 (2017) 827–838.

[8] M.R. Bafandeh, R. Gharahkhani, M.H. Fathi, Characterization of fabricated cobalt-based alloy/nano bioactive glass composites, Mater. Sci. Eng. C Mater. Biol. Appl. 69 (2016) 692–699.

[9] Y. Zeng, X. Pei, S. Yang, H. Qin, H. Cai, S. Hu, et al., Graphene oxide/hydroxyapatite composite coatings fabricated by electrochemical deposition, Surf. Coating. Technol. 286 (2016) 72–79.

[10] P. Haji Mohammadi Gohari, M. Haghbin Nazarpak, M. Solati-Hashjin, The effect of adding reduced graphene oxide to electrospun polycaprolactone scaffolds on MG-63 cells activity, Mater. Today Commun. 27 (2021), 102287.

[11] B. Ranishenka, E. Ulashchik, M. Tatulchenkov, O. Sharko, A. Panarin, N. Dremova, et al., Graphene oxide functionalization via epoxide ring opening in bioconjugation compatible conditions, FlatChem 27 (2021), 100235.

[12] E.A. Lee, S.-Y. Kwak, J.-K. Yang, Y.-S. Lee, J.-H. Kim, H.D. Kim, et al., Graphene oxide film guided skeletal muscle differentiation, Mater. Sci. Eng. C 126 (2021), 112174.

[13] C. Yao, J. Zhu, A. Xie, Y. Shen, H. Li, B. Zheng, et al., Graphene oxide and creatine phosphate disodium dual template-directed synthesis of GO/hydroxyapatite and its application in drug delivery, Mater. Sci. Eng. C Mater. Biol. Appl. 73 (2017) 709–715.

[14] Y.C. Shin, J.H. Lee, O.S. Jin, S.H. Kang, S.W. Hong, B. Kim, et al., Synergistic effects of reduced graphene oxide and hydroxyapatite on osteogenic differentiation of MC3T3-E1 preosteoblasts, Carbon 95 (2015) 1051–1060.

[15] R.M. Mohammed, Effect of antimony oxide nanoparticles on structural, optical and AC electrical properties of (PEO-PVA) blend for antibacterial applications, Int. J. Emerg. Trends Eng. Res. 8 (2020) 4726–4738.

[16] Y. Zhao, J. Xu, Z. Li, T. Fu, S. Jiang, In vitro antibacterial properties of MoO3/SiO2/Ag2O nanocomposite coating prepared by double cathode glow discharge technique, Surf. Coating. Technol. 397 (2020), 125992.

[17] N. Fifere, A. Airinei, M. Dobromir, L. Sacarescu, S.I. Dunca, Revealing the effect of synthesis conditions on the structural, optical, and antibacterial properties of cerium oxide nanoparticles, Nanomaterials (2021) 11.

[18] W. Adamson, C. Jia, Y. Li, C. Zhao, Cobalt oxide micro flowers derived from hydrothermal synthesised cobalt sulphide pre-catalyst for enhanced water oxidation, Electrochim. Acta 355 (2020), 136802.

[19] N. Akhlaghi, G. Najafpour-Darzi, H. Younesi, Facile and green synthesis of cobalt oxide nanoparticles using ethanolic extract of Trigonella foenumgraceum (Fenugreek) leaves, Adv. Powder Technol. 31 (2020) 3562–3569.

[20] A. Bhattacharjee, A. Gupta, M. Verma, M.P. Anand, P. Sengupta, M. Saravanan, et al., Antibacterial and magnetic response of site-specific cobalt incorporated hydroxyapatite, Ceram. Int. 46 (2020) 513–522.

[21] N. Fairley, V. Fernandez, M. Richard-Plouet, C. Guillot-Deudon, J. Walton, E. Smith, et al., Systematic and collaborative approach to problem solving using X-ray photoelectron spectroscopy, Appl. Surface Sci. Adv. 5 (2021), 100112.

[22] J.H. Scofield, HARTREE-SLATER SUBSHELL PHOTOIONIZATION CROSS-SECTIONS AT 1254 AND 1487 eV, J. Electron. Spectrosc. Relat. Phenom. 8 (1976) 8.

[23] W. Shao, J. He, F. Sang, B. Ding, L. Chen, S. Cui, et al., Coaxial electrospun aligned tussah silk fibroin nanostructured fiber scaffolds embedded with hydroxyapatite-tussah silk fibroin nanoparticles for bone tissue engineering, Mater. Sci. Eng. C Mater. Biol. Appl. 58 (2016) 342–351.

[24] J. Zou, J.-F. Guan, G.-Q. Zhao, X.-Y. Jiang, Y.-P. Liu, J.-G. Yu, et al., Construction of a highly sensitive signal electrochemical sensor based on self-assembled cobalt oxide-hydroxylated single-walled carbon nanotubes composite for detection of dopamine in bovine serum samples, J. Environ. Chem. Eng. 9 (2021), 105831.

[25] S.H. Alwan, H.A.H. Alshamsi, L.S. Jasim, Rhodamine B removal on A-rGO/cobalt oxide nanoparticles composite by adsorption from contaminated water, J. Mol. Struct. 1161 (2018) 356–365.

[26] M. Aadil, S. Zulfiqar, H. Sabeeh, M.F. Warsi, M. Shahid, I.A. Alsafari, et al., Enhanced electrochemical energy storage properties of carbon coated Co3O4 nanoparticles-reduced graphene oxide ternary nano-hybrids, Ceram. Int. 46 (2020) 17836–17845.

[27] S. Dayan, Performance improvement of Co3O4@nHAP hybrid nanomaterial in the UV light-supported degradation of organic pollutants and photovoltaics as counter electrode, J. Mol. Struct. 1238 (2021), 130390.

[28] F.A.J. Al-Doghachi, U. Rashid, Z. Zainal, M.I. Saiman, Y.H. Taufiq Yap, Influence of Ce2O3 and CeO2 promoters on Pd/MgO catalysts in the dry-reforming of methane, RSC Adv. 5 (2015) 81739–81752.

[29] A. Amari, Electrochemical and optical properties of tellurium dioxide (TeO2) nanoparticles, Int. J. Electrochem. Sci. (2021), 210235.

[30] R. Verma, S.K. Samdarshi, S. Bojja, S. Paul, B. Choudhury, A novel thermophotocatalyst of mixed-phase cerium oxide (CeO2/Ce2O3) homocomposite nanostructure: role of interface and oxygen vacancies, Sol. Energy Mater. Sol. Cell. 141 (2015) 414–422.

[31] V.P. Padmanabhan, R. Kulandaivelu, G. Devendrapandi, S. Vivekananthan, S. Suresh, A. Lett, Microwave synthesis of hydroxyapatite encumbered with

ascorbic acid intended for drug leaching studies, Mater. Res. Innovat. 24 (2019) 1–8.
[32] A. Abdal-hay, N. Abbasi, M. Gwiazda, S. Hamlet, S. Ivanovski, Novel polycaprolactone/hydroxyapatite nanocomposite fibrous scaffolds by direct melt-electrospinning writing, Eur. Polym. J. 105 (2018) 257–264.
[33] N. Abdolhi, A. Soltani, H.K. Fadafan, V. Erfani-Moghadam, A.D. Khalaji, H. Balakheyli, Preparation, characterization and toxicity evaluation ofCo3O4and NiO-filled multi-walled carbon nanotubes loaded to chitosan, Nano-Struct. Nano-Objects 12 (2017) 182–187.
[34] G. Asha, V. Rajeshwari, G. Stephen, S. Gurusamy, D. Carolin Jeniba Rachel, Eco-friendly synthesis and characterization of cobalt oxide nanoparticles by sativum species and its photo-catalytic activity, Mater. Today: Proc. 48 (2021) 486–493.
[35] Z. Çiplak, N. Yildiz, A. Çalimli, Investigation of graphene/Ag nanocomposites synthesis parameters for two different synthesis methods, Fullerenes, Nanotub. Carbon Nanostruct. 23 (2015) 361–370.
[36] L.-H. Ai, J. Jiang, Rapid synthesis of nanocrystalline Co3O4 by a microwave-assisted combustion method, Powder Technol. 195 (2009) 11–14.
[37] J.D. Afroze, M.J. Abden, M.A. Islam, An efficient method to prepare magnetic hydroxyapatite-functionalized multi-walled carbon nanotubes nanocomposite for bone defects, Mater. Sci. Eng. C Mater. Biol. Appl. 86 (2018) 95–102.
[38] I.L. Ardelean, D. Gudovan, D. Ficai, A. Ficai, E. Andronescu, M.G. Albu-Kaya, et al., Collagen/hydroxyapatite bone grafts manufactured by homogeneous/ heterogeneous 3D printing, Mater. Lett. 231 (2018) 179–182.
[39] Y. Zhang, L. Zhou, Y. Liu, D. Liu, F. Liu, F. Liu, et al., Gas sensor based on samarium oxide loaded mulberry-shaped tin oxide for highly selective and sub ppm-level acetone detection, J. Colloid Interface Sci. 531 (2018) 74–82.
[40] M.C. Biesinger, B.P. Payne, A.P. Grosvenor, L.W.M. Lau, A.R. Gerson, R.S.C. Smart, Resolving surface chemical states in XPS analysis of first row transition metals, oxides and hydroxides: Cr, Mn, Fe, Co and Ni, Appl. Surf. Sci. 257 (2011) 2717–2730.
[41] R. Courtney, J.B. Usher, Vicki H. Grassian, Spatially resolved product formation in the reaction of formic acid with calcium carbonate (101h4): the role of step density and adsorbed water-assisted ion mobility, Langmuir : ACS J. Surfaces Colloids 23 (2007) 6.
[42] F. Foroughi, S.A. Hassanzadeh-Tabrizi, J. Amighian, Microemulsion synthesis and magnetic properties of hydroxyapatite-encapsulated nano CoFe2O4, J. Magn. Magn Mater. 382 (2015) 182–187.
[43] C. Shuai, B. Peng, P. Feng, L. Yu, R. Lai, A. Min, In situ synthesis of hydroxyapatite nanorods on graphene oxide nanosheets and their reinforcement in biopolymer scaffold, J. Adv. Res. 35 (2021) 13–24.
[44] J. Jyoti, A. Kiran, M. Sandhu, A. Kumar, B.P. Singh, N. Kumar, Improved nanomechanical and in-vitro biocompatibility of graphene oxide-carbon nanotube hydroxyapatite hybrid composites by synergistic effect, J. Mech. Behav. Biomed. Mater. 117 (2021), 104376.
[45] K. Krishnamoorthy, N. Umasuthan, R. Mohan, J. Lee, S.-J. Kim, Antibacterial activity of graphene oxide nanosheets, Sci. Adv. Mater. 4 (2012) 1111–1117.
[46] A. El-Fiqi, H.-W. Kim, Sol-gel synthesis and characterization of novel cobalt ions-containing mesoporous bioactive glass nanospheres as hypoxia and ferroptosis-inducing nanotherapeutics, J. Non-Cryst. Solids 569 (2021), 120999.
[47] J. Dobosz, M. Małecka, M. Zawadzki, Hydrogen generation via ethanol steam reforming over Co/HAp catalysts, J. Energy Inst. 91 (2018) 411–423.
[48] Huang Xiao, S.B. Christopher, On the importance and mechanisms of burstrelease in matrix-controlled drug delivery systems, J. Contr. Release : Off. J. Contr. Release Soc. 73 (2001) 121–136.
[49] A. Mazinani, M.J. Nine, R. Chiesa, G. Candiani, P. Tarsini, T.T. Tung, et al., Graphene oxide (GO) decorated on multi-structured porous titania fabricated by plasma electrolytic oxidation (PEO) for enhanced antibacterial performance, Mater. Des. 200 (2021), 109443.
[50] Z. Pei, Z. Zhang, G. Li, F. Fu, K. Zhang, Y. Cai, et al., Improvement of in vitro osteogenesis and antimicrobial activity of injectable brushite for bone repair by incorporating with Se-loaded calcium phosphate, Ceram. Int. 47 (2021) 11144–11155.
[51] S.C. Veerla, D.R. Kim, J. Kim, H. Sohn, S.Y. Yang, Controlled nanoparticle synthesis of Ag/Fe co-doped hydroxyapatite system for cancer cell treatment, Mater. Sci. Eng. C 98 (2019) 311–323.
[52] M. Kaushik, R. Niranjan, R. Thangam, B. Madhan, V. Pandiyarasan, C. Ramachandran, et al., Investigations on the antimicrobial activity and wound healing potential of ZnO nanoparticles, Appl. Surf. Sci. 479 (2019) 1169–1177.
[53] M. Paul Das, J. Rebecca Livingstone, P. Veluswamy, J. Das, Exploration of Wedelia chinensis leaf-assisted silver nanoparticles for antioxidant, antibacterial and in vitro cytotoxic applications, J. Food Drug Anal. 26 (2018) 917–925.
[54] D.T. de Castro, M.L. Valente, C.H. da Silva, E. Watanabe, R.L. Siqueira, M. A. Schiavon, et al., Evaluation of antibiofilm and mechanical properties of new nanocomposites based on acrylic resins and silver vanadate nanoparticles, Arch. Oral Biol. 67 (2016) 46–53.
[55] G. Wang, G. Qian, J. Zan, F. Qi, Z. Zhao, W. Yang, et al., A co-dispersion nanosystem of graphene oxide @silicon-doped hydroxyapatite to improve scaffold properties, Mater. Des. 199 (2021), 109399.
[56] N.A. Saad, Enhanced the antibacterial and mechanical properties of UHMWPE by addition sort fibers of polyacrylonitraile PAN, graphene nanoplate (GNP) and hydroxyapatite (HAp), Indian J. Forensic Med. Toxicol. 14 (2020) 1370–1376.